



# Concepts for long-baseline high-mass matter-wave interferometry\*

Filip Kiałka<sup>1</sup>, Benjamin A Stickler<sup>1</sup>, Klaus Hornberger<sup>1</sup> ,  
Yaakov Y Fein<sup>2</sup>, Philipp Geyer<sup>2</sup>, Lukas Mairhofer<sup>2</sup>, Stefan Gerlich<sup>2</sup> and  
Markus Arndt<sup>2</sup> 

<sup>1</sup>Faculty of Physics, University of Duisburg-Essen, Lotharstraße 1, D-47048 Duisburg, Germany

<sup>2</sup>Faculty of Physics, University of Vienna, Boltzmanngasse 5, A-1090 Vienna, Austria

E-mail: [markus.arndt@univie.ac.at](mailto:markus.arndt@univie.ac.at)

Received 28 June 2018, revised 10 October 2018

Accepted for publication 20 November 2018

Published 24 January 2019



CrossMark

## Abstract

Designing experiments which delocalize ever more complex and more massive particles requires a quantitative assessment of new interferometer configurations. Here, we introduce a figure of merit which quantifies the difference between a genuine quantum interference pattern and a classical shadow and use it to compare a number of near-field interferometer schemes. This allows us to identify the most promising setups for future tests of the quantum superposition principle, and to discuss the perspectives of interferometry with complex molecules and clusters.

Keywords: matter wave optics, quantum optics in phase space, interferometry with clusters and molecules

(Some figures may appear in colour only in the online journal)

## 1. Introduction

Matter-wave interference is a prominent example of fundamental quantum physics, with applications in quantum sensing and metrology [1, 2]. On the fundamental side, it is a direct test of the universality of the superposition principle and its possible breakdown beyond a certain mass and complexity limit [3–5]. Matter-wave interferometry has been used for quantum-enhanced measurements of gravitational effects [6–11] and in the search for dark energy [12]. Nanoparticle interferometry can enable new quantum tests of the weak equivalence principle [7, 13–15] in a range of internal particle properties and masses that cannot be compared in any other device so far [16]. Moreover, it has been suggested that certain candidates for dark matter might be best detected in nanoparticle interferometry [17, 18]. Matter-wave interference

experiments of the future aim to probe gravity-induced dephasing and decoherence [19–22, 26], and to test predictions of the Newton–Schrödinger equation [23] or the quantum nature of gravity [24, 25]. Interestingly, the influence of these phenomena tends to grow with the square of the mass of the delocalized particle. This also holds for a recent definition of macroscopicity, which quantifies the degree to which nonlinear extensions of quantum mechanics can be excluded [27].

On the applied side, a matter-wave interference pattern can be thought of as a free-flying nanometric ruler, the displacement of which can be measured with high sensitivity. In atom interferometry, this enables precise measurement of accelerations, such as those arising due to rotation or gravity [28–30]. Based on the same principle, macromolecule and nanoparticle interferometry can be developed for force sensing and used to measure molecular properties [31, 32]. This has been used to probe optical [33] and static [34] molecular polarizability, dipole moments [35], absolute optical absorption cross sections [36], and to distinguish molecular conformers [37, 38]. Extended to large peptides and proteins, such techniques can become a valuable tool for biophysical chemistry.

\* This special issue is honoring the 60th birthday of Wolfgang Schleich. Our contribution relates closely to his seminal research and teaching on quantum physics in phase space.



Original content from this work may be used under the terms of the [Creative Commons Attribution 3.0 licence](https://creativecommons.org/licenses/by/3.0/). Any further distribution of this work must maintain attribution to the author(s) and the title of the work, journal citation and DOI.

The instruments representing the state of the art in high-mass matter-wave physics are the Kapitza–Dirac–Talbot–Lau interferometer (KDTLI) [39] and the optical time-domain matter interferometer (OTIMA). KDTLI demonstrated quantum interference of bio-dyes, vitamins [34], and hot molecules with masses beyond 10 000 Da [40]. It was also used for many of the metrological applications mentioned above [33, 35, 37, 38]. OTIMA has demonstrated interference with molecular clusters [41, 42] and recently of molecules with masses beyond 6000 Da [16].

Both KDTLI and OTIMA rely on the near-field self-imaging of a diffractive element known as the Talbot–Lau effect [43, 44]. It is a two-grating phenomenon, in which the first grating prepares spatial coherence and the subsequent grating acts as the diffractive element. The Talbot–Lau scheme is especially suitable for high-mass interference because of the lack of bright coherent sources for molecules and clusters. Talbot–Lau interference is well-known in optics [45–47], has been demonstrated with atoms [48], and is also the basis for our present discussion. For a diffractive element with period  $d$ , the self-images occur at integer multiples of the Talbot length,  $L_T = d^2/\lambda_{dB}$ , where  $\lambda_{dB}$  is the de Broglie wavelength of the particle. The definition of  $L_T$  implies that pushing towards higher masses requires developments in slowing and cooling of heavy particles, but also an increase of the interferometer length. This motivates the present study of the long-baseline universal matter-wave interferometer, an instrument that is ten times longer than the current mass-record holder, the KDTLI. The goal of the new interferometer is to probe de Broglie wavelengths down to  $\lambda_{dB} = 20\text{--}30$  fm and demonstrate interference of masses beyond  $10^5$  Da.

The article is structured as follows: in section 2 we review the phase-space description of near-field interference, and derive a figure of merit that is later used to compare different interferometer setups. In section 3 we identify and discuss the most promising interferometer schemes for organic molecules, proteins, and atomic and molecular clusters. We end with a summary in section 4.

## 2. Phase-space description of near-field matter-wave interferometry

In this section, we describe the propagation of matter waves through a near-field interferometer and quantify the resulting interference pattern. We consider two- and three-grating setups and provide both a quantum and a classical description. Comparing these predictions is necessary to identify parameter ranges where quantum interference fringes are clearly distinguishable from a classical shadow [49].

Both descriptions are performed in the phase space  $(x, p)$  of the particle's motion in the direction perpendicular to the grating slits and the particle beam. We assume that the particle's forward motion can be separated and is thus constant, with velocity  $v$ . We further assume that the gratings are aligned to gravity, so that the particle falls freely along the grating slits. Gravity then only shifts the vertical position of the pattern, but does not reduce the fringe contrast.

The phase-space description allows us to derive the classical and quantum predictions based on the same approximations, and to insert the various beam-splitting components discussed in section 3. The phase-space description can also be extended to include decoherence events during free flight [50], measurement-induced beam splitting [51], and various metrological agents such as externally applied fields [34].

### 2.1. Quantum description

The transverse motional quantum state  $\hat{\rho}$  of the particle of mass  $m$  is represented with a Wigner function defined as [52]

$$w(x, p) = \frac{1}{2\pi\hbar} \int ds e^{ips/\hbar} \left\langle x - \frac{s}{2} \left| \hat{\rho} \right| x + \frac{s}{2} \right\rangle. \quad (1)$$

Assuming that the source uniformly illuminates an  $X_0$ -wide area of the first grating and that the momentum distribution in the beam is  $D(p)$ , the initial state can be written as

$$w_0(x, p) = \frac{D(p)}{X_0} \theta\left(\frac{X_0}{2} - |x|\right), \quad (2)$$

where  $\theta(x)$  is the Heaviside step function. After traversing the first grating, the state becomes

$$w_1(x, p) = \int dp_0 \mathcal{T}_1(x, p - p_0) w_0(x, p_0), \quad (3)$$

where the transformation kernel  $\mathcal{T}_1(x, p)$  is a Wigner transform of the first grating's transmission function  $t_1(x)$  calculated using the eikonal approximation [53]

$$\mathcal{T}_1(x, p) = \frac{1}{2\pi\hbar} \int ds e^{ips/\hbar} t_1\left(x - \frac{s}{2}\right) t_1^*\left(x + \frac{s}{2}\right). \quad (4)$$

Between the first and second grating, the molecule propagates for a time  $T_1$  under the influence of an external force causing transverse acceleration  $a$ . This corresponds to a transformation of the form

$$w_1'(x, p) = w_1\left(x - \frac{p}{m}T_1 + \frac{aT_1^2}{2}, p - maT_1\right). \quad (5)$$

For the second grating and second propagation, analogous transformations are performed, yielding  $w_2'(x, p)$ .

In a two-grating interferometer the particle is then detected using a spatially-resolving detector. The probability density of detection at position  $x$  is

$$P(x) = \int dp w_2'(x, p). \quad (6)$$

In the wide-illumination limit  $X_0 \rightarrow \infty$ , the probability density  $P(x)$  approaches a periodic function with a Fourier decomposition

$$P(x) = \frac{1}{X_0} \sum_{n=-\infty}^{\infty} \exp\left(-2\pi i n \frac{T_1}{T_2} x\right) P_n. \quad (7)$$

The  $P_n$  can be expressed in terms of the Fourier coefficients  $B_n^{(i)}(\xi)$  of the transformation kernels  $\mathcal{T}_i(x, p)$ . For the  $i$ th grating with period  $d_i$  and  $n \in \mathbb{Z}$ , these coefficients are

defined as

$$B_n^{(i)}(\xi) = \frac{1}{d_i} \int_0^{d_i} dx \int dp e^{-2\pi i n x / d_i - i p \xi d_i / \hbar} \mathcal{T}_i(x, p) \quad (8)$$

and taken to be 0 for  $n \notin \mathbb{Z}$ . Assuming that the width of  $D(p)$  is much greater than the grating momenta  $\hbar/d_i$  (and that  $X_0 \rightarrow \infty$ ),  $P_n$  can be expressed as [53]

$$P_n = e^{2\pi i \varphi_n} B_n^{(1)}(0) B_{-n(T_1+T_2)d_2/(T_2d_1)}^{(2)} \left( -n \frac{\hbar T_1}{m d_1 d_2} \right), \quad (9)$$

where  $\hbar$  is the Planck constant and the phase shift due to external force is

$$\varphi_n = \frac{n a (T_1 + T_2) T_1}{2 d_1}. \quad (10)$$

In all cases considered in this paper the acceleration will be due to the Coriolis force

$$a = 2\Omega_{\parallel} v, \quad (11)$$

where  $\Omega_{\parallel}$  is the vertical component of Earth's angular velocity at the lab's latitude and  $v$  is the forward velocity of the molecule<sup>3</sup>.

A three-grating interferometer has one more grating after the second propagation, which can be moved perpendicularly to the fringes. This allows one to detect the presence of the pattern by measuring the flux of the transmitted particles as a function of the transverse position  $x_S$  of the last grating. This is useful because many detection techniques lack the spatial resolution sufficient for direct imaging of the interference pattern.

The probability that the molecule transverses a three-grating interferometer is

$$S(x_S) = \int dx dp dp_2 \mathcal{T}_3(x - x_S, p - p_2) w_2'(x, p_2). \quad (12)$$

In the wide-illumination limit  $X_0 \rightarrow \infty$ , the signal approaches a periodic function with a Fourier decomposition

$$S(x_S) = \sum_{n=-\infty}^{\infty} \exp\left(-2\pi i n \frac{T_1 x_S}{T_2 d_1}\right) S_n. \quad (13)$$

$S_n$  can be expressed as [53]

$$S_n = P_n B_{n T_1 d_3 / (T_2 d_1)}^{(3)}(0). \quad (14)$$

## 2.2. Classical description

In the classical description, the state of the particle is described with a phase-space probability distribution  $f(x, p)$ . Before the first grating,  $f$  coincides with  $w_0$ , given in equation (2). Upon traversing a grating,  $f$  undergoes a transformation of the same form as given in equation (3), but with a classical kernel  $\mathcal{K}_1(x, p)$  instead of  $\mathcal{T}_1(x, p)$

$$\mathcal{K}_1(x, p) = |t_1(x)|^2 \delta(p - q_1(x)), \quad (15)$$

where  $q_1(x)$  is the momentum kick experienced by the particle traversing the first grating at position  $x$  [53].

Using a decomposition of  $\mathcal{K}_i(x, p)$  analogous to equation (8) with coefficients denoted  $C_n^{(i)}$ , we can express the Fourier coefficients of the classical pattern and signal in a form analogous to equations (9) and (14), but with  $B_n^{(i)}$  replaced by  $C_n^{(i)}$  [50]. These coefficients will be denoted  $P_n^{\text{cl}}$  and  $S_n^{\text{cl}}$ , respectively.

## 2.3. Figure of merit

A primary goal of an interference experiment with massive particles is to demonstrate their quantum behavior by producing a fringe pattern significantly more pronounced than predicted by classical theory. To quantify how well an interferometer performs at this task, we will calculate the difference between the quantum and the classical fringe modulation and compare it to the relevant noise scale<sup>4</sup>.

We assume that the particle detection rate in the absence of gratings is constant and equal to  $N/T$ , where  $T$  is the total data-taking time. In a two-grating interferometer, the mean number of counts registered in a pixel of size  $\Delta x$  is then

$$N \Delta x \langle P(x) \rangle. \quad (16)$$

The averaging of the probability density  $P(x)$  is done over the distribution of the velocities in the beam, and we have assumed that  $\Delta x$  is smaller than the length scale at which  $P(x)$  varies appreciably. Using equation (7) to expand  $P(x)$  we find that the difference between the amplitude of  $n$ th order fringes as predicted by quantum and classical theory is

$$\frac{2N \Delta x}{X_0} (| \langle P_n \rangle | - | \langle P_n^{\text{cl}} \rangle |). \quad (17)$$

The noise in our measurements is due to Poissonian counting statistics and its standard deviation can be estimated as<sup>5</sup>

$$\frac{\Delta x}{X_0} \sqrt{N P_0}. \quad (18)$$

This noise is identical in the quantum and classical models and velocity-independent, hence no averaging is necessary.

We define our figure of merit as the number of counts  $N$  for which the amplitudes of the lowest-order quantum and classical fringes differ by two shot noise amplitudes.  $N$  can then be obtained by equating the ratio of expressions (17) and (18) to 2, yielding

$$N = \frac{P_0}{(| \langle P_n \rangle | - | \langle P_n^{\text{cl}} \rangle |)^2}, \quad (19)$$

where  $n$  is the smallest index such that  $P_n \neq 0$ . In a three-grating interferometer, the integration is done in time bins,

<sup>4</sup> It should be noted that for purely metrological purposes this figure of merit is less relevant. In that case the key parameters are fringe visibility and count rate.

<sup>5</sup> The standard deviation of the number of counts in a single pixel is approximately  $\sqrt{N \Delta x P_0 / X_0}$ . Since we have  $X_0 / \Delta x$  independent pixels, the noise is reduced by a factor of  $\sqrt{X_0 / \Delta x}$ , which gives equation (18).

<sup>3</sup> The horizontal component of Earth's rotation, which depends on the azimuthal orientation of the interferometer, gives rise to a Coriolis force acting along the grating slits and therefore can be neglected.

between which the third grating is moved. By reasoning analogously as above, we arrive at an expression for  $N$  of the same form as equation (19), but with  $P_n, P_n^{\text{cl}}$  replaced by  $S_n, S_n^{\text{cl}}$ .

The main purpose of the figure of merit  $N$  is to compare the performance of interferometer setups. However, we can also use it as a guide when estimating the number of counts each scheme requires in order to produce a manifestly quantum fringe pattern. These experimentally relevant count numbers are most likely one to two orders of magnitude higher than  $N$ . The additional counts are necessary to offset the imperfections which we neglected in this analysis, such as residual grating vibration and misalignment or non-ionizing photon absorption for biomolecules. Also, a signal-to-noise ratio significantly higher than two is often desired, especially if the experiment is to exclude modifications of quantum mechanics despite significant uncertainty in molecular parameters.

### 3. Long-baseline interferometers for molecules and clusters

In this section, we compare the most promising configurations of a two meter long interferometer for the diffraction of proteins, as well as of metal and amino acid clusters, using the figure of merit  $N$  of section 2.

#### 3.1. Grating types

We consider three types of diffraction gratings: nano-machined masks, optical phase gratings, and optical depletion gratings (see figure 1). The Talbot coefficients  $B_n$  and  $C_n$  (see equation (8)) for these grating types can be found in [53].

**3.1.1. Material masks.** A *material grating* ( $M$ ) is a thin nanostructured membrane, which serves to modulate the matter wavefront of atoms, molecules, and clusters alike. This type of grating is the most universal, but suffers from the dispersive influence of the Casimir–Polder (CP) interaction between the particles and the slit wall<sup>6</sup>. When the material mask is used as the middle grating, this leads to strong blurring of the interference pattern [56]. Therefore, we will only consider material masks for the outer gratings, for which the CP-interaction can be approximated as a reduction of the effective slit width [57, 58], as discussed in appendix B. Motivated by previous high-mass experiments [36], we will assume silicon nitride gratings with a period of  $d = 266$  nm.

**3.1.2. Optical phase gratings.** A *phase grating* ( $P$ ) can be realized as a standing wave of laser light, which imprints a periodic phase onto the matter-wave via the dipole interaction [39, 59]. This type of grating is perfectly transmissive, does not clog, and is compatible with high-mass interference despite the dependence of the imprinted phase on the particle's velocity [60]. However, the outer gratings will

<sup>6</sup> In naming the dispersion forces, we follow the nomenclature of [55].

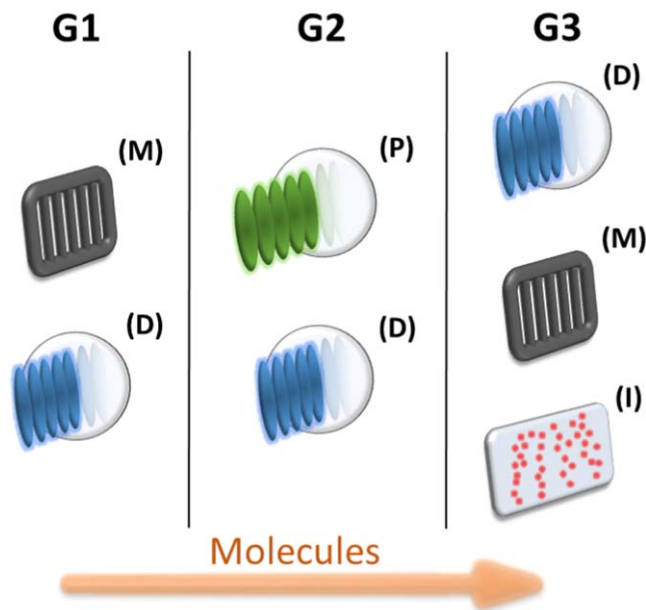


**Figure 1.** The interferometer configurations in this survey consist of up to three gratings, based on up to three different mechanisms. The first grating ( $G1$ ) must be absorptive to establish spatial coherence. It can be realized as material mask ( $M$ ) or a standing light wave depleting the molecular beam ( $D$ ). The second grating ( $G2$ ) can be a pure phase grating ( $P$ ). Interference detection can be achieved either by scanning an absorptive grating ( $G3$ ), or by direct imaging ( $I$ ) of the molecules deposited on a surface. In our study  $M$  and  $P$  gratings are defined to have a period of 266 nm, while  $D$  gratings have half the period.

always be assumed to be absorptive masks, as required to prepare coherence ( $G1$ ) and to analyze the resulting density pattern ( $G3$ ).

In our analysis, we assume 532 nm light for a phase grating with period  $d = 266$  nm. For highly transparent dielectric materials, such as  $\text{SiO}_2$  spheres, this period could be further reduced by a factor of two by using UV light.

**3.1.3. Optical depletion gratings.** A *photo-depletion grating* ( $D$ ) can be implemented as a standing light wave which ionizes [41] or dissociates [61] the particles passing near its anti-nodes. Provided that only the neutral or intact particles are counted, these photo-processes lead to periodic molecular beam depletion. This idea can be applied to tryptophan clusters [62], a vast range of biomolecules [63], and many metal clusters [64]. In cases where the ionization energy exceeds the available photon energy, photo-cleavage ionization can be implemented by appropriate functionalization of the molecules [54]. Photo-fragmentation gratings are also expected to work for beams of native RNA and DNA [65], which undergo intense fragmentation upon UV irradiation. Depletion gratings may also be realized via optical transfer of the particles to undetectable internal states, which removes them from the detected ensemble without actually depleting the molecular beam [66, 67]. In our analysis, we assume a 266 nm UV-light depletion grating, which yields a period of 133 nm.

**Table 1.** Molecules and clusters used in this study and their parameters: polarizability volumes  $\alpha$  and absorption cross sections  $\sigma$  at 266 and 532 nm. The absorption cross sections of insulin and GFP correspond to that of the photo-cleavable group [54]. The remaining values are estimated as described in appendix A.

	$m$ (kDa)	$\alpha_{266}$ ( $\text{\AA}^3$ )	$\sigma_{266}$ ( $\text{cm}^2$ )	$\alpha_{532}$ ( $\text{\AA}^3$ )	$\sigma_{532}$ ( $\text{cm}^2$ )
Insulin	5.8	600	$4 \times 10^{-17}$	600	0
Trp <sub>50</sub> [68]	10	1000	$9.1 \times 10^{-16}$	1000	0
GFP <sup>a</sup>	27	2700	$4 \times 10^{-17}$	2700	0
Silver	100	2500	$6.9 \times 10^{-15}$	5200	$2.1 \times 10^{-16}$
Cesium	100	-2200	$6.5 \times 10^{-15}$	-22000	$2.4 \times 10^{-14}$
Silver	300	7400	$2.1 \times 10^{-14}$	15400	$6.2 \times 10^{-16}$
Cesium	300	-6700	$1.9 \times 10^{-14}$	-65000	$7.2 \times 10^{-14}$

<sup>a</sup> Green fluorescent protein.

### 3.2. Particle species, sources, and detectors

We analyze various interferometer configurations in combination with seven prototypical biomolecules, amino acid clusters and metal clusters (see table 1). This is an exemplary and certainly not exhaustive list of potential candidates up to 300 000 Da. Biomolecules are especially interesting for metrological purposes, while metal clusters or certain dielectric nanoparticles promise the simplest implementation of photo-depletion gratings and are suitable for high-mass interference.

One of the greatest challenges in matter-wave experiments is preparing a sufficiently intense, mass-selected, cold, and directed particle beam. While many native and functionalized organic molecules—from fullerenes and tailored tripeptides [69] to native vitamins [34]—can still be evaporated in a Knudsen cell, molecular beams of complex amino acid clusters and high-mass polypeptides can be prepared by laser desorption into a noble gas jet [70]. We expect that photo-neutralization of singly charged biopolymers [54] and aggregated metal clusters [71] will facilitate the preparation of neutral particle beams.

On the detector side, a key challenge is to efficiently ionize neutral massive particles. While hot-wire detection [72] is a simple and efficient tool for metal clusters with a low work function, single-photon ionization offers high efficiency for a larger range of metals and allows for excellent time resolution. Post-ionization of large amino acid clusters [62] has been observed but the detection of neutral proteins has remained a grand challenge in physical chemistry [73]. This is being tackled using functionalization and photo-cleavage [54].

In most molecule interferometers to date, ionizing detectors count the molecules transmitted through the interferometer and the required spatial resolution is provided by scanning a grating across the interference pattern. For some setups in this study, we propose instead the adsorption of the interferogram on a transparent surface, followed by high resolution imaging using electron or optical super-resolution microscopy [74–76].

### 3.3. Survey results

In order to compare the interferometer setups we numerically compute and optimize the figure of merit  $N$  (see

equation (19)) for each combination of grating configuration and particle species. The optimization is carried out over the average velocity of the particles and the powers of the laser gratings. For configurations with multiple laser gratings, the powers of the outer gratings are held equal. The results are summarized in figure 2.

For the biomolecules in our list, we find that all of the setups considered offer similar performance. The greatest difference can be seen between the imaging and the inter-grating-detection setups, the latter typically requiring about an order of magnitude<sup>7</sup> more counts to achieve the same degree of distinguishability between the classical and the quantum model. Within both groups, optimal performance is offered by the material-depletion setups (MDM and MDI), followed closely by the material-phase (MPM and MPI) and the asymmetric depletion-phase configurations (DPM 1:2 and DPI 1:2). The MPM configuration is close to optimal among these setups. The DPM 1:2 and DPI 1:2 setups are the best alternatives should clogging of the material grating become a problem. The calculated values of  $N$  suggest that all proposed setups are viable with biomolecules if one can detect and accumulate a total of several ten thousand molecular counts.

For 100 kDa metal clusters we find that, similar to biomolecules, the material-depletion setups offer the best performance. Also, replacing the last grating with a spatially-resolving detector has again the effect of lowering the required numbers of counts by about an order of magnitude. We find that some configurations are better for silver than for cesium, because of the high polarizability of the cesium cluster at 532 nm. In that case the best discrimination between the quantum and the classical model would nominally be achieved at low velocities, where for the same reason a material grating becomes almost opaque. This is especially pronounced for the setups MPM and MPI with a material grating in  $G1$  and a phase grating in  $G2$ . All considered setups are viable with 100 kDa silver clusters for a few hundred

<sup>7</sup> The exact factor can be estimated analytically in the following way. Note that the removal of the last grating improves the transmission of the interferometer by  $1/B_0^{(3)}(0)$ , while the pattern amplitude changes by  $1/B_{n\tilde{I}d_3/(T_2d_1)}^{(3)}(0)$  in the quantum and by  $1/C_{n\tilde{I}d_3/(T_2d_1)}^{(3)}(0)$  in the classical model (see equation (14)). One can show that  $B_k^{(3)}(0) = C_k^{(3)}(0)$  and therefore, when  $B_k^{(3)}$  is velocity-independent or when the velocity spread is small,  $N$  changes by a factor  $[B_{n\tilde{I}d_3/(T_2d_1)}^{(3)}(0)]^2/B_0^{(3)}(0)$ .

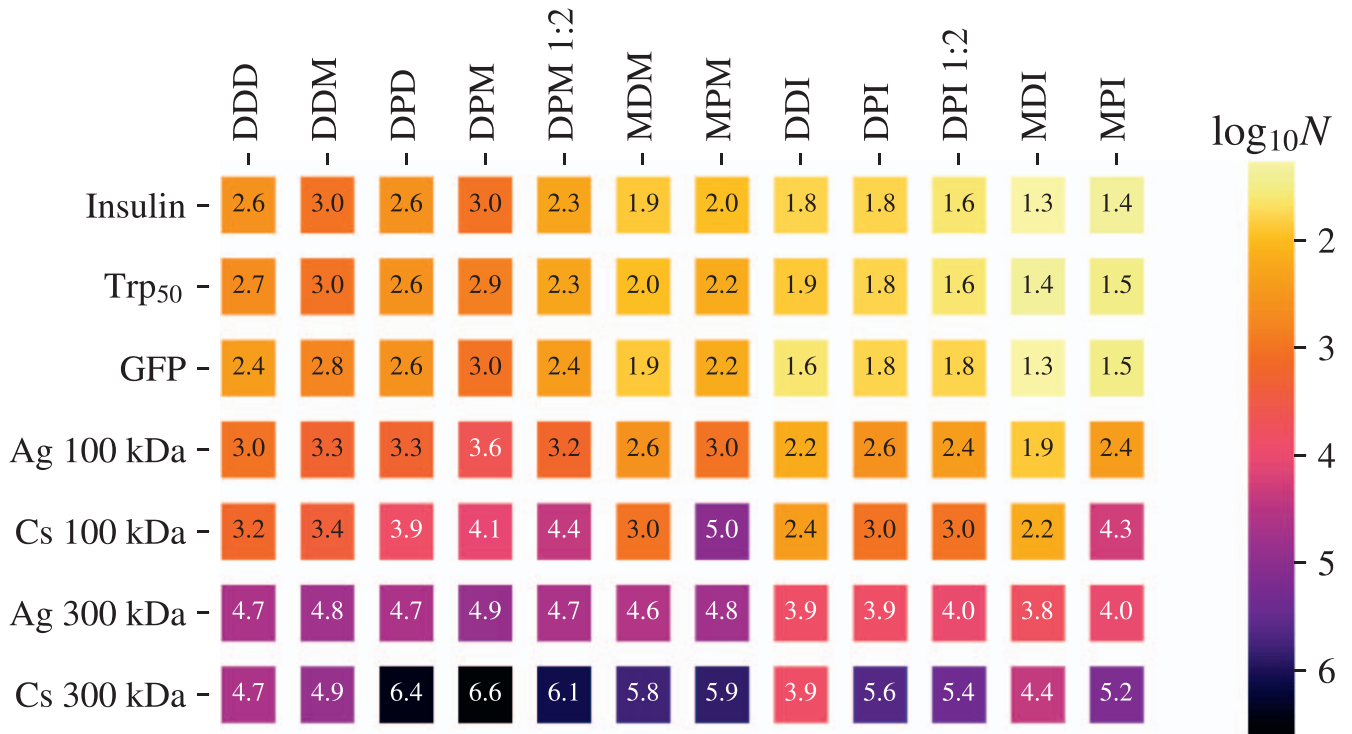


**Figure 2.** Distinguishability of the quantum and the (hypothetical) classical pattern for various interferometer configurations and particle species, as quantified by the count number  $N$  of equation (19) (smaller is better).  $D$ ,  $M$ , and  $P$  stand for depletion, material, and phase grating, respectively, and the letter  $I$  denotes spatially-resolving detection; e.g. by fluorescence imaging of surface-adsorbed molecules. The numbers following the setup names specify the ratio of distances between the gratings,  $L_1 = \overline{G1G2}$  and  $L_2 = \overline{G2G3}$ , with  $L_1:L_2 = 1:1$  if not otherwise mentioned. These results are obtained assuming a Gaussian velocity spread in the particle beam with a standard deviation equal to 5% of the average velocity. The latter is optimized for minimal  $N$  over the 30–600 m s<sup>-1</sup> range.

thousand counts. This also holds for 100 kDa cesium clusters if  $G2$  is a depletion grating.

For clusters with a mass of 300 000 Da an imaging interferometer can achieve the same discrimination between a quantum and a classical model as a non-imaging scheme, but it achieves that feat with ten times fewer counts. The high polarizability of the cesium clusters is even more apparent here, significantly affecting the performance of all configurations with a phase grating in  $G2$ . For 300 kDa silver clusters a few million counts will be required, when the Coriolis force is not compensated.

In all cases considered, the asymmetric depletion-phase-material (DPM 1:2) performs better than its symmetric counterpart. Because of the longer distance between  $G2$  and  $G3$ , low-order diffraction at  $G2$  is already sufficient to close the interferometer paths at  $G3$ . This is true for all Talbot–Lau interferometers with unequal grating periods.

Figure 2 suggests that the minimal number of counts required to verify the quantumness of the fringe pattern increases with the mass of the particle. This is due to the dephasing caused by the Coriolis force, which is proportional to mass if the interferometer length is fixed. This can be seen from equations (10) and (11) assuming the total transit time is proportional to the Talbot time  $T_T = md^2/h$ . If the Coriolis force is compensated, the particle mass can be increased

without loss of distinguishability as long as the laser power and the particle’s polarizability and velocity are adjusted accordingly.

In the discussion above we assumed that for each setup the optimal laser intensity can be reached. For insulin and GFP we require more than 20 W of UV light for a laser beam focused to a  $1/e^2$  waist of  $w = 150 \mu\text{m}$ . This is challenging but within reach of intracavity UV power enhancement. For metal clusters, laser intensities as low as 1 W at 266 nm or 15 W at 532 nm are sufficient, even at a waist of  $750 \mu\text{m}$ . These power levels are readily available from commercial light sources.

#### 4. Summary and outlook

Our results suggest that the MPM configuration, as used in the earlier KDTLI interferometer [77] can be suitable for quantum interference of biomolecules as complex as the green fluorescent protein at 27 000 Da (see figure 3) or even silver clusters beyond 300 000 Da, if the interferometer is stretched by a factor of ten to  $L_1 = L_2 = 1\text{m}$ . The arguments in favor of metal clusters also hold for silicon nanoparticles, which may eventually even be prepared by advanced cavity cooling methods in a mass range of  $10^6$ – $10^7$  Da [78].

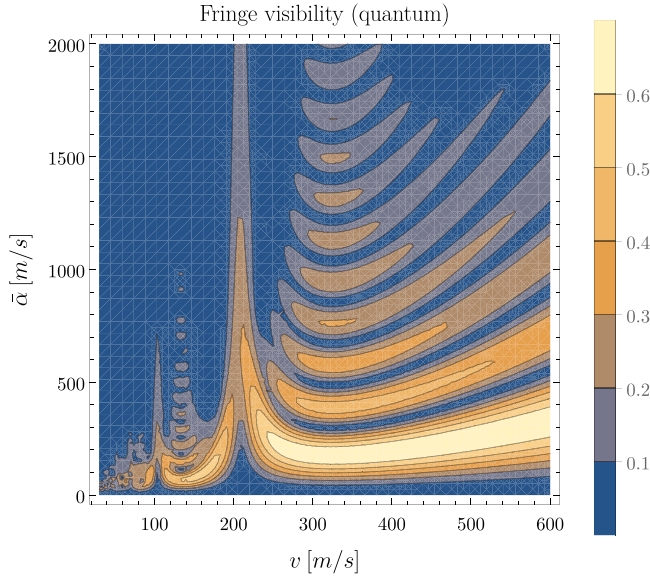


**Figure 3.** Visibility of green fluorescent protein (GFP) interference fringes in a material-phase-material grating interferometer, as predicted by the quantum model. In the notation of equation (13), the visibility is defined as  $2|S_n|/S_0$ , where  $n$  is the smallest value for which  $S_n \neq 0$ . The velocity distribution in the beam is assumed to be Gaussian with mean  $v$  and  $0.05v$  standard deviation.  $\bar{\alpha}$  is a measure of the strength of particle-grating interaction, defined as  $\bar{\alpha} = 8\sqrt{2\pi}\alpha P/(hcw_z)$ , where  $\alpha$  is the polarizability volume,  $P$  is laser power,  $w_z$  is the  $1/e^2$  intensity radius of the beam in the direction of the molecules' propagation, and  $h$ ,  $c$  are the Planck constant and the velocity of light. The phase acquired by particles moving with velocity  $v$  through the antinode of the standing laser wave is then  $2\pi\bar{\alpha}/v$ . Note, that GFP does not fluoresce in the unsolvated vacuum state, nor can it be photo-ionized using standard techniques. We thus assume that UV photo-cleavage ionization of a small tag can be used [54].

The survey also allows us to identify alternative schemes to overcome foreseeable experimental challenges en route to those goals. The alternative setups include the asymmetric depletion-phase configurations (DPM 1:2 and DPI 1:2), where the nanomask in  $G1$  is substituted by a UV standing light wave and  $G3$  can either be a mechanical grating or an adsorptive surface which is subsequently imaged. Photo-depletion gratings are advisable when clogging of the material mask becomes a limitation. The DDD and DDI configurations are furthermore advantageous over MPM and MDM for high-mass interference, for instance with cesium.

A major constraint to high-mass interference is the dephasing due to the Coriolis force, which can be mitigated in a figure-eight setup, as demonstrated for atoms [79, 80].

For each interferometer setup, we have found the molecular velocity and laser power that minimize the number of counts required to distinguish a quantum fringe pattern from a classical moire effect. Optimal performance can be achieved when the last grating is replaced by a single-particle imaging detector based on fluorescence [76], STED [81], or highly sensitive scattering imaging for particles beyond about 10 000 Da [82, 83].

These findings will guide future experimental efforts in high-mass interferometry.

## Acknowledgments

This project has received funding from the European Research Council (ERC) under the European Union's Horizon 2020 research and innovation program (Grant Nr. 320694), the Austrian Science Funds within FWF COLMI (P30176), and FWF CoQuS (W 1210-N25).

## Appendix A. Polarizabilities and cross sections of biomolecules and clusters

In the following, we briefly describe how we estimate the polarizability volumes and absorption cross sections shown in table 1. These quantities enter the coefficients  $B_n^{(i)}$  and  $C_n^{(i)}$  describing the particle-grating interaction.

For biomolecules, we use their static polarizabilities, which we estimate by summing the contributions of aromatic amino acids (including histidine), assuming that each contributes  $20 \text{ \AA}^3$ , and non-aromatic amino acids, assuming that each contributes  $10 \text{ \AA}^3$ . To estimate the absorption cross section, we first estimate the molar absorption coefficient  $\varepsilon$  as in [84]. The cross section is then obtained as

$$\sigma = \frac{\varepsilon \log 10}{N_A}, \quad (\text{A1})$$

where  $N_A$  is the Avogadro number.

Polarizabilities for clusters are estimated based on the experimental values of the real and imaginary part of the complex refractive index [85, 86]. Using those, we calculate the relative permittivity  $\varepsilon$  and then the polarizability volume and absorption cross section using the formulas for a sub-wavelength dielectric sphere [53]

$$\alpha = r^3 \text{Re} \frac{\varepsilon - 1}{\varepsilon + 2}, \quad (\text{A2})$$

$$\sigma = \frac{8\pi^2 r^3}{\lambda} \text{Im} \frac{\varepsilon - 1}{\varepsilon + 2}. \quad (\text{A3})$$

where  $\lambda$  is the wavelength and  $r$  is the radius of the cluster estimated using the number of atoms and the Wigner–Saitz radii taken from [87, 88].

## Appendix B. Effective opening fraction of material gratings

To estimate the effective slit width in the presence of particle-grating interaction, we assume that the particles which get deflected by more than a fixed angle  $\theta_c$  remain undetected. If the interaction potential is  $V(x)$  and  $b$  is the grating's thickness, the deflection angle to first order in the grating transit time is

$$\theta \approx -\frac{V'(x)b}{mv^2}. \quad (\text{B1})$$

Equation (B1) is a good approximation as long as the higher order term is negligible; that is, as long as

$$\frac{V''(x)v^2 m - (V')^2(x)\left(\frac{b}{v}\right)^2}{6m^2v^2} \ll 1. \quad (\text{B2})$$

Substituting the CP potential for  $V(x)$  yields the cutoff distance for a particle with static polarizability volume  $\alpha_0$

$$x_c = \left( \frac{12C_\varepsilon \hbar c \alpha_0 b}{8\pi m v^2 \theta_c} \right)^{\frac{1}{5}}, \quad (\text{B3})$$

where [55]

$$C_\varepsilon = \int_1^\infty d\nu \left[ \left( \frac{2}{\nu^2} - \frac{1}{\nu^4} \right) \frac{\varepsilon\nu - \sqrt{\varepsilon\mu - 1 + \nu^2}}{\varepsilon\nu + \sqrt{\varepsilon\mu - 1 + \nu^2}} - \frac{1}{\nu^4} \frac{\mu\nu - \sqrt{\varepsilon\mu - 1 + \nu^2}}{\mu\nu + \sqrt{\varepsilon\mu - 1 + \nu^2}} \right] \quad (\text{B4})$$

is a constant depending on the static relative permittivities  $\varepsilon$  and  $\mu$  of the grating material. Knowing  $x_c$ , we can calculate the effective opening fraction  $f'$  from the physical value  $f$ .

$$f' = f - \frac{2x_c}{d}. \quad (\text{B5})$$

Using  $f'$ , we can express the Talbot coefficients of the material gratings as [53]

$$B_n(0) = C_n(0) = f' \text{sinc}(\pi n f'). \quad (\text{B6})$$



Many molecules also possess permanent electric dipole moments. Their influence can be estimated using the orientation-averaged, non-retarded potential of a dipole  $D$  in the vicinity of a dielectric half-space

$$V_{D\varepsilon}(x) = -\frac{\varepsilon - 1}{\varepsilon + 1} \frac{D^2}{48\pi\varepsilon_0} \frac{1}{x^3}. \quad (\text{B7})$$

To do this, we take the potential in equation (B1) to be the sum of the dipole potential (B7) and the CP potential.

Assuming parameters similar to those used in previous high-mass experiments [36] ( $f = 0.42$ ,  $\varepsilon = 7.5$  and  $\mu = 1$  for silicon nitride,  $b = 100$  nm, and  $\theta_c = 0.5$  mrad) and the prototypical particles listed in table 1, we find that the influence of the CP interaction is significant at slow velocities ( $v \approx 100$  m s<sup>-1</sup>), often reducing the opening fraction by a factor of two. We further find that, although the dipole and the CP potentials can be comparable, including the former changes  $f'$  only by few percent points. This is because of the very steep dependence of both forces, and thus the deflection angle  $\theta$ , on the particle-grating distance. The contribution of the permanent dipole moments to the particle-grating interaction is therefore neglected in the present analysis.

## ORCID iDs

Klaus Hornberger  <https://orcid.org/0000-0002-3145-1117>  
Markus Arndt  <https://orcid.org/0000-0002-9487-4985>

## References

- [1] Cronin A D, Schmiedmayer J and Pritchard D E 2009 *Rev. Mod. Phys.* **81** 1051
- [2] Tino G M and Kasevich M A 2014 *Atom Interferometry* vol 188 (Amsterdam: IOS Press)
- [3] Rosen N 1964 *Am. J. Phys.* **32** 597
- [4] Bassi A, Lochan K, Satin S, Singh T and Ulbricht H 2013 *Rev. Mod. Phys.* **85** 471
- [5] Arndt M and Hornberger K 2014 *Nat. Phys.* **10** 271
- [6] Colella R, Overhauser A W and Werner S A 1975 *Phys. Rev. Lett.* **34** 1472
- [7] Tarallo M G, Mazzone T, Poli N, Sutyryn D V, Zhang X and Tino G M 2014 *Phys. Rev. Lett.* **113** 023005
- [8] Müntinga H et al 2013 *Phys. Rev. Lett.* **110** 093602
- [9] Nesvizhevsky V V et al 2002 *Nature* **415** 298
- [10] Schlippert D, Hartwig J, Albers H, Richardson L L, Schubert C, Roura A, Schleich W P, Ertmer W and Rasel E M 2014 *Phys. Rev. Lett.* **112** 203002
- [11] Asenbaum P, Overstreet C, Kovachy T, Brown D D, Hogan J M and Kasevich M A 2017 *Phys. Rev. Lett.* **118** 183602
- [12] Hamilton P, Jaffe M, Haslinger P, Simmons Q, Müller H and Khoury J T 2015 *Science* **349** 849
- [13] Schlippert D, Hartwig J, Albers H, Richardson L L, Schubert C, Roura A, Schleich W P, Ertmer W and Rasel E M 2014 *Phys. Rev. Lett.* **112** 203002
- [14] Bonnin A, Zahzam N, Bidet Y and Bresson A 2013 *Phys. Rev. A* **88** 043615
- [15] Zhou L et al 2015 *Phys. Rev. Lett.* **115** 013004
- [16] Rodewald J, Dörre N, Grimaldi A, Geyer P, Felix L, Mayor M, Shayeghi A and Arndt M 2018 *New J. Phys.* **20** 033016
- [17] Riedel C J and Yavin I 2017 *Phys. Rev. D* **96** 023007
- [18] Riedel C J 2015 *Phys. Rev. A* **92** 010101(R)
- [19] Pikovski I, Zych M, Costa F and Brukner C 2015 *Nat. Phys.* **11** 668
- [20] Diosi L 1984 *Phys. Lett. A* **105** 199
- [21] Penrose R 1996 *Gen. Rel. Grav.* **28** 581
- [22] Lamine B, Hervé R, Lambrecht A and Reynaud S 2006 *Phys. Rev. Lett.* **96** 050405
- [23] Giulini D and Großardt A 2013 Gravitationally induced inhibitions of dispersion according to a modified Schrödinger–Newton equation for a homogeneous-sphere potential *Class. Quantum Grav.* **30** 155018
- [24] Bose S, Mazumdar A, Morley G W, Ulbricht H, Toros M, Paternostro M, Geraci A A, Barker P F, Kim M S and Milburn G 2017 *Phys. Rev. Lett.* **119** 240401
- [25] Marletto C and Vedral V 2017 *Phys. Rev. Lett.* **119** 240402
- [26] Bonifacio P M, Wang C H T, Mendonça J T and Bingham R 2009 *Class. Quantum Grav.* **26** 145013
- [27] Nimmrichter S and Hornberger K 2013 *Phys. Rev. Lett.* **110** 160403
- [28] Gustavson T L, Landragin A and Kasevich M A 2000 *Class. Quantum Grav.* **17** 2385
- [29] Geiger R et al 2011 *Nat. Commun.* **2** 474
- [30] Dutta I, Savoie D, Fang B, Venon B, Garrido Alzar C L, Geiger R and Landragin A 2016 *Phys. Rev. Lett.* **116** 183003
- [31] Hornberger K, Gerlich S, Haslinger P, Nimmrichter S and Arndt M 2012 *Rev. Mod. Phys.* **84** 157
- [32] Arndt M 2014 *Phys. Today* **67** 30
- [33] Hackermüller L, Hornberger K, Gerlich S, Gring M, Ulbricht H and Arndt M 2007 *Appl. Phys. B* **89** 469
- [34] Mairhofer L, Eibenberger S, Cotter J P, Romirer M, Shayeghi A and Arndt M 2017 *Angew. Chem., Int. Ed.* **56** 10947
- [35] Eibenberger S, Gerlich S, Arndt M, Tüxen J and Mayor M 2011 *New J. Phys.* **13** 043033



- [36] Eibenberger S, Cheng X, Cotter J P and Arndt M 2014 *Phys. Rev. Lett.* **112** 250402
- [37] Gerlich S, Gring M, Ulbricht H, Hornberger K, Tüxen J, Mayor M and Arndt M 2008 *Angew. Chem., Int. Ed.* **47** 6195
- [38] Tüxen J, Gerlich S, Eibenberger S, Arndt M and Mayor M 2010 *Chem. Commun.* **46** 4145
- [39] Gerlich S et al 2007 *Nat. Phys.* **3** 711
- [40] Eibenberger S, Gerlich S, Arndt M, Mayor M and Tüxen J 2013 *Phys. Chem. Chem. Phys.* **15** 14696
- [41] Haslinger P, Dörre N, Geyer P, Rodewald J, Nimmrichter S and Arndt M 2013 *Nat. Phys.* **9** 144
- [42] Dörre N, Rodewald J, Geyer P, von Issendorff B, Haslinger P and Arndt M 2014 *Phys. Rev. Lett.* **113** 233001
- [43] Talbot W H F 1836 *Phil. Mag.* **9** 401
- [44] Lau E 1948 *Ann. Phys.* **437** 417
- [45] Patorski K 1989 *Progress in Optics* ed E Wolf vol 27 (Amsterdam: Elsevier) ch 1 pp 1–108
- [46] Berry M, Marzoli I and Schleich W 2001 *Phys. World* **14** 39
- [47] Kazemi P, Chaturvedi S, Marzoli I, O'Connell R F and Schleich W P 2013 *New J. Phys.* **15** 013052
- [48] Clauser J F and Li S 1994 *Phys. Rev. A* **49** R2213
- [49] Batelaan H, Bernet S, Oberthaler M K, Rasel E M, Schmiedmayer J and Zeilinger A 1997 Classical and quantum atom fringes *Atom Interferometry* ed P R Berman (New York: Academic)
- [50] Hornberger K, Sipe J E and Arndt M 2004 *Phys. Rev. A* **70** 053608
- [51] Cotter J P, Eibenberger S, Mairhofer L, Cheng X, Asenbaum P, Arndt M, Walter K, Nimmrichter S and Hornberger K 2015 *Nat. Commun.* **6** 7336
- [52] Schleich W P 2011 *Quantum Optics in Phase Space* (New York: Wiley)
- [53] Nimmrichter S 2013 Macroscopic matter-wave interferometry *PhD Thesis* University of Vienna
- [54] Debiossac M, Schatti J, Kriegleder M, Geyer P, Shayeghi A, Mayor M, Arndt M and Köhler V 2018 *Phys. Chem. Chem. Phys.* **20** 11412
- [55] Buhmann S Y 2012 *Dispersion Forces I (Springer Tracts in Modern Physics)* vol 247 1st edn (Berlin: Springer)
- [56] Brezger B, Arndt M and Zeilinger A 2003 *J. Opt. B* **5** S82
- [57] Grisenti R E, Schöllkopf W, Toennies J P, Hegerfeldt G C, Köhler T and Stoll M 2000 *Phys. Rev. Lett.* **85** 2284
- [58] Brand C et al 2015 *Nat. Nanotechnol.* **10** 845–8
- [59] Nairz O, Brezger B, Arndt M and Zeilinger A 2001 *Phys. Rev. Lett.* **87** 160401
- [60] Eibenberger S, Gerlich S, Arndt M, Mayor M and Tüxen J 2013 *Phys. Chem. Chem. Phys.* **15** 14696
- [61] Dörre N, Rodewald J, Geyer P, von Issendorff B, Haslinger P and Arndt M 2014 *Phys. Rev. Lett.* **113** 233001
- [62] Marksteiner M, Haslinger P, Sclafani M, Ulbricht H and Arndt M 2009 *J. Phys. Chem. A* **113** 9952
- [63] Polfer N C and Dugourd P 2015 *Laser Photodissociation and Spectroscopy of Mass-Separated Biomolecular Ions* (Berlin: Springer)
- [64] Sattler K D 2011 *Handbook of Nanophysics: Clusters and Fullerenes* (Boca Raton, FL; London: CRC Press; Taylor and Francis)
- [65] Gabelica V, Rosu F, Pauw E D, Antoine R, Tabarin T, Broyer M and Dugourd P 2007 *J. Am. Soc. Mass Spectrom.* **18** 1990
- [66] Abfalterer R, Keller C, Bernet S, Oberthaler M K, Schmiedmayer J and Zeilinger A 1997 *Phys. Rev. A* **56** R4365
- [67] Fray S, Diez C A, Hänisch T W and Weitz M 2004 *Phys. Rev. Lett.* **93** 240404
- [68] Marksteiner M, Haslinger P, Ulbricht H, Sclafani M, Oberhofer H, Dellago C and Arndt M 2008 *J. Am. Soc. Mass Spectrom.* **19** 1021
- [69] Schätti J, Sezer U, Pedalino S, Cotter J P, Arndt M, Mayor M and Köhler V 2017 *J. Mass Spectrom.* **52** 550
- [70] Geyer P, Sezer U, Rodewald J, Mairhofer L, Dörre N, Haslinger P, Eibenberger S, Brand C and Arndt M 2014 *Phys. Scr.* **91** 063007
- [71] Haberland H, Karrais M and Mall M 1991 *Z. Phys. D* **20** 413
- [72] Taylor J B and Langmuir I 1933 *Phys. Rev.* **44** 423
- [73] Hanley L and Zimmermann R 2009 *Anal. Chem.* **81** 4174
- [74] Hell S W and Wichmann J 1994 *Opt. Lett.* **19** 780
- [75] Betzig E, Patterson G H, Sougrat R, Lindwasser O W, Olenych S, Bonifacino J S, Davidson M W, Lippincott-Schwartz J and Hess H F 2006 *Science* **313** 1642
- [76] Juffmann T, Milic A, Müllneritsch M, Asenbaum P, Tsukernik A, Tüxen J, Mayor M, Cheshnovsky O and Arndt M 2012 *Nat. Nanotechnol.* **7** 297
- [77] Gerlich S, Eibenberger S, Tomandl M, Nimmrichter S, Hornberger K, Fagan P, Tüxen J, Mayor M and Arndt M 2011 *Nat. Commun.* **2** 263
- [78] Kuhn S, Wachter G, Wieser F-F, Millen J, Schneider M, Schalko J, Schmid U, Trupke M and Arndt M 2017 *Appl. Phys. Lett.* **111** 253107
- [79] Clauser J F 1989 *NASA Conf. Publication* vol 3046 ed R W Hellings
- [80] McGuirk J M, Foster G T, Fixler J B, Snadden M J and Kasevich M A 2002 *Phys. Rev. A* **65** 033608
- [81] Hell S W and Wichmann J 1994 *Opt. Lett.* **19** 780
- [82] Piliarik M and Sandoghdar V 2014 *Nat. Commun.* **5** 4495
- [83] Tzang O, Pevzner A, Marvel R E, Haglund R F and Cheshnovsky O 2015 *Nano Lett.* **15** 1362
- [84] Pace C N, Vajdos F, Fee L, Grimsley G and Gray T 1995 *Protein Sci.* **4** 2411
- [85] Lynch D W and Hunter W 1997 *Handbook of Optical Constants of Solids* ed E D Palik (Burlington, MA: Academic) pp 275–367
- [86] Inagaki T and Arakawa E 1997 *Handbook of Optical Constants of Solids* ed E D Palik (Burlington, MA: Academic) pp 341–50
- [87] Limberger H G and Martin T P 1989 *J. Chem. Phys.* **90** 2979
- [88] Ashcroft N and Mermin N 1976 *Solid State Physics* (San Diego, CA: Harcourt College Publishers)